Mechanical Systems and Signal Processing 85 (2017) 468–486

Contents lists available at ScienceDirect

Mechanical Systems and Signal Processing

journal homepage: www.elsevier.com/locate/ymssp

Bayesian characterization of buildings using seismic interferometry on ambient vibrations

Hao Sun [a], Aurélien Mordret [b], Germán A. Prieto [b], M. Nafi Toksöz [b], Oral Büyüköztürk [a,*]

[a] Department of Civil and Environmental Engineering, MIT, Cambridge, MA 02139, USA
[b] Department of Earth, Atmospheric and Planetary Science, MIT, Cambridge, MA 02139, USA

ARTICLE INFO

Article history:
Received 31 March 2016
Received in revised form
26 July 2016
Accepted 28 August 2016

Keywords:
Probabilistic model updating
Bayesian inference
Seismic interferometry
Building impulse response
Ambient vibration
Markov chain Monte Carlo

ABSTRACT

Continuous monitoring of engineering structures provides a crucial alternative to assess its health condition as well as evaluate its safety throughout the whole service life. To link the field measurements to the characteristics of a building, one option is to characterize and update a model, against the measured data, so that it can best describe the behavior and performance of the structure. In this paper, we present a novel computational strategy for Bayesian probabilistic updating of building models with response functions extracted from ambient noise measurements using seismic interferometry. The intrinsic building impulse response functions (IRFs) can be extracted from ambient excitation by deconvolving the motion recorded at different floors with respect to the measured ambient ground motion. The IRF represents the representative building response to an input delta function at the ground floor. The measurements are firstly divided into multiple windows for deconvolution and the IRFs for each window are then averaged to represent the overall building IRFs. A hierarchical Bayesian framework with Laplace priors is proposed for updating the finite element model. A Markov chain Monte Carlo technique with adaptive random-walk steps is employed to sample the model parameters for uncertainty quantification. An illustrative example is studied to validate the effectiveness of the proposed algorithm for temporal monitoring and probabilistic model updating of buildings. The structure considered in this paper is a 21-storey concrete building instrumented with 36 accelerometers at the MIT campus. The methodology described here allows for continuous temporal health monitoring, robust model updating as well as post-earthquake damage detection of buildings.

1. Introduction

Vibration-based structural health monitoring (SHM) provides a primary tool for evaluating structural condition, integrity and reliability as well as for assessing potential risks throughout the lifecycle of structures. In recent years, topics on health monitoring of buildings have drawn great attention (to name a few, [1–10], among others). The vibrational measurements of the building can be responses induced by earthquake, ambient, or man-controlled excitations. Modal analysis of the vibrational records is commonly carried out to extract building characteristics such as damping ratios, resonant frequencies

* Corresponding author.
E-mail addresses: haosun@mit.edu (H. Sun), obuyuk@mit.edu (O. Büyüköztürk).

http://dx.doi.org/10.1016/j.ymssp.2016.08.038
0888-3270/

and mode shapes, using system identification techniques such as stochastic subspace identification [11], frequency domain decomposition [12], blind source separation [13], Bayesian operational modal analysis (OMA) [14–20], etc. It is worthwhile to mention that recent advances in Bayesian OMA showed that robust posterior probabilistic distributions of the modal parameters can be determined for given data and modeling assumptions without involving any stochastic averaging concept (see the work by Yuen et al. [14], Au et al. [15–18] and others [19,20] for example). The identified modal properties are then used for structural condition evaluation, model updating, and post-earthquake damage detection, etc.

Different from OMA widely used in building monitoring, Snieder and Şafak [21] proposed a deconvolution-based seismic interferometry approach to separate the impulse response functions (IRFs) of the building from the source of excitation and from the soil-structure interaction. The IRFs illustrate the propagation of shear waves (e.g., attenuation and scattering) inside the building, which are substantially composed of the building intrinsic characteristics such as the wave velocity, attenuation factor, resonant frequencies, mode shapes, etc. This approach has proven to be a successful and powerful technique for building monitoring under earthquake excitation, especially in one dimension (e.g., the translational direction) [22,3,23–25,9]. The IRFs as well as the associated characteristics are useful for building condition assessment. Nevertheless, the deconvolution interferometry mentioned above relies on natural source excitations such as earthquakes, which limits its applicability to continuous temporal health monitoring of buildings.

Recently, Prieto et al. [26] extended the deconvolution-based seismic interferometry approach to process a long duration of ambient noise measurements using a temporal averaging technique. The ambient vibration records were divided into overlapping windows and deconvolved with respect to a reference record window-by-window. Temporal averaging of the extracted waveforms for each window yields the overall IRFs of the building. This approach was successfully tested on the instrumented Factor building located at the campus of the University of California, Los Angeles. In another study, Nakata and Snieder [23] applied the deconvolution interferometry to the ambient vibration data of a building in Japan and obtained both causal and acausal waves propagating in the building for both positive and negative times. A string model was developed to quantitatively interpret the deconvolved IRFs. However, this model maybe too simple to describe the building's mechanical characteristics, and to be used for damage detection purposes. Similar to the OMA techniques (see [17] for example), the deconvolution interferometry method does not require knowledge of the input sources but assuming that they are statistically random when ambient noise data is used. Compared to the OMA methods, a distinctive feature of the interferometry approach is that the phase information can be well extracted for shear wave velocity estimation. Nevertheless, to remove the source effect using temporal averaging, the deconvolution interferometry approach requires a sufficiently long data set (see Section 2.1), which limits this approach to be applied to short period ambient measurements.

In this paper, we employ the extracted IRFs to update the finite element model of a building. The objective is to establish a baseline model, calibrated against field records, for building response prediction subjected to potential extreme events and for damage detection/quantification in future operations of the building. The majority of existing work in literature on model updating with output-only measurements such as ambient vibration records are based on structural modal parameters, e.g., frequencies, mode shapes, and frequency response functions (see [27–37] for example). In these approaches, the modal properties are commonly identified from the output-only measurements using OMA techniques mentioned previously and mode matching is performed in most cases. In general, the model updating strategies can be categorized into two groups, namely, deterministic vs. probabilistic. The deterministic approaches (e.g., constrained optimization [38,31,32], sensitivity method [39–41], heuristic optimization [28,42]) aim to tune parameters so that the updated model can best predict the measured data, while the probabilistic methods use Bayesian inference and make possible to identify a set of plausible models with probabilistic distributions and to characterize the modeling uncertainties [29,30,43,34,44–46,35–37,47]. For example, Au and Zhang [48,49] proposed a two-stage formulation successfully applied to Bayesian modal identification and updating of structural model parameters using ambient vibration data.

Instead of using the modal quantities, we herein apply the hierarchical Bayesian inference to update the finite element model of a building against the IRFs extracted from ambient vibration records using deconvolution interferometry. The model parameters are quantified using a Markov chain Monte Carlo (MCMC) technique with adaptive random-walk steps for sampling. Straightforward response (IRFs) matching at observation locations is recursively performed in the Bayesian updating process for given modeling assumptions.

This paper is organized as follows. Section 2 presents the deconvolution interferometry approach for building response extraction using ambient vibration records. Section 3 describes the probabilistic model updating framework based on hierarchical Bayesian inference and the MCMC sampling technique with adaptive random-walk steps for parameter uncertainty quantification. In Section 4, a 21-storey concrete building instrumented with 36 accelerometers at the MIT campus is studied to validate the performance of the proposed approach for continuous monitoring and model updating of buildings. Finally, Section 5 gives the discussions and conclusions.

2. Extracting building response using seismic interferometry

The vibration of a building is related to the excitation, the soil-structure interaction, and the building mechanical properties [21]. Separating the building response from the excitation and the soil-structure interaction using vibrational data yields information of the intrinsic characteristics of the building. We herein apply a seismic interferometric method to extract the shear waves propagating in the building, identical to the IRFs, based on deconvolution [21,22,3,26,50,23,24]. The

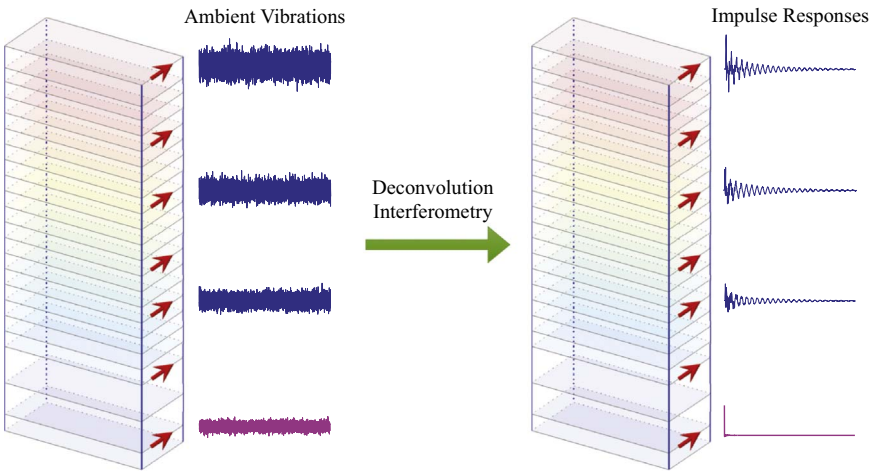

Fig. 1. Schematic representation of extracting building's impulse responses using convolution-based seismic interferometry on ambient vibrational measurements. (For interpretation of the references to color in this figure legend, the reader is referred to the web version of this article.)

IRF represents the representative building response to an input delta function at the reference level. Treating the ground (or basement) record as the reference measurement, the IRFs of the building can be computed as follows [23]

$$S(z,\,t) \approx \sum_{n=1}^{N}\left[\mathcal{F}^{-1}\left\{\frac{y_n(z,\,\omega)y_n^*(z_0,\,\omega)}{\left|y_n(z_0,\,\omega)\right|^2 + \delta\langle\left|y_n(z_0,\,\omega)\right|^2\rangle}\right\}\right] \tag{1}$$

where $S(z,\,t)$ is the IRF at z (the floor level, $z \le H$, with H being the building height); $y_n(z,\,\omega)$ is the nth wavefield at z in the frequency domain; $\langle|y_n|^2\rangle$ is the average power spectrum of y_n; ω is the angular frequency; t is the time; z_0 is the reference level of the building (e.g., the ground or the basement);* denotes the complex conjugate; N is the total number of time intervals of the measurements; δ is a stabilizing parameter (water level), e.g., $\delta = 0.005$ in this study; $\mathcal{F}^{-1}$ denotes the inverse Fourier transform.

2.1. Extracting IRFs using ambient noise measurement

When earthquake records are used, the IRFs can be directly extracted using Eq. (1) by treating the ground motion measurement as the source. In temporal monitoring of buildings, ambient noise measurements are typically recorded and used for building response estimation. For ambient vibrations, it has been shown that, if the vibration sources are homogeneously distributed around and inside the building, the deconvolution between signals recorded at different floors will be the IRF of the portion located between the two sensors [26]. In this case, temporal averaging can be applied [23,26]. We first assume that the ambient noise measurements have a sufficient duration (e.g., Prieto et al. [26] suggested the data length is greater than two weeks with a typical sampling rate of 50~200 Hz for building monitoring). The ambient records excluding large amplitude data are then divided into multiple overlapping windows (e.g., 10–20 min windows, overlapping 50%) and the IRFs of each window are extracted with respect to the reference source location by deconvolution using Eq. (1). Finally, the building IRFs are estimated by averaging the deconvolved traces for each window, which is equivalent to temporal averaging. Temporal averaging over an enough long duration for numerous random sources ensures a sufficient uniform source distribution [26,51]. Fig. 1 shows a schematic representation of extracting building's impulse responses using convolution-based seismic interferometry on ambient vibrational measurements.

2.2. Estimating wave speed, damping parameter and mode shapes

Based on the extracted IRFs, we can estimate the travel time (t_v) of the seismic shear wave from the reference source location to the top of the building. The shear wave velocity V can be calculated by the height of the building (H) divided by the travel time (t_v), namely, $V = H/t_v$. In addition, for each resonant frequency, the damping ratio can be calculated from the amplitude delay with time. The IRFs are first filtered around the resonant frequency within the half-power bandwidth. The envelopes of the filtered IRFs are then calculated and fitted by linear lines whose slopes are used to determine the damping ratio corresponding to the resonant frequency. To wit, the damping ratio ξ_r can be calculated as follows

$$\xi_r = \frac{1}{N_o \omega_r} \sum_{i=1}^{N_o} |\mu_i| \tag{2}$$

where ω_r is the rth resonant frequency, N_o is the number of observations, μ_i is the slope of the envelop for the ith observation location. The filtered IRFs within the half-power bandwidth of a dominant frequency can be also used to calculate the mode shape of the corresponding mode. For a certain mode, the mode shape values are obtained through peaking the values of the filtered storey IRFs at zero time ($t=0$).

3. Probabilistic model updating

The successful identification of the building IRFs makes possible to characterize the physical properties such as stiffness parameters of a model against the extracted time histories of IRFs. The essential promise of structural model updating conditional on the IRFs is to quantify a set of model parameters (e.g., denoted with $\boldsymbol{\theta} \in \mathbb{R}^{N_\theta \times 1}$, where N_θ is the number of parameters) that minimize the discrepancy between the predicted and the extracted IRFs. For example, we consider a linear building model with N_θ degrees-of-freedoms (DOFs). The mass matrix $\mathbf{M} \in \mathbb{R}^{N_\theta \times N_\theta}$ is assumed to be known and the stiffness matrix $\mathbf{K} \in \mathbb{R}^{N_\theta \times N_\theta}$ is parameterized by $\boldsymbol{\theta}$, namely,

$$\mathbf{K} = \mathbf{K}_0 + \sum_{l}^{N_\theta} \theta_l \mathbf{K}_l \tag{3}$$

where $\mathbf{K}_0$ denotes an initial stiffness matrix which can be derived from a full scale finite element model for a building; $\mathbf{K}_l$ is a nominal substructure contribution to the global stiffness matrix ($l = 1, 2, \ldots, N_\theta$). We herein propose a hierarchical Bayesian framework for estimating the unknown model parameters.

3.1. Hierarchical bayesian modeling

In the framework of Bayesian model updating, the posterior probability density function (PDF) of $\boldsymbol{\theta}$ can be obtained based on the Bayes' theorem:

$$p(\boldsymbol{\theta}|\mathcal{D}) = \frac{p(\mathcal{D}|\boldsymbol{\theta}) p(\boldsymbol{\theta})}{p(\mathcal{D})} \tag{4}$$

where $p(\mathcal{D})$ is called the evidence written as follows

$$p(\mathcal{D}) = \int_{\Theta} p(\mathcal{D}|\boldsymbol{\theta}) p(\boldsymbol{\theta}) \mathrm{d}\boldsymbol{\theta} \tag{5}$$

Here, Θ represents the domain of integration; $p(\boldsymbol{\theta}|\mathcal{D})$ denotes the posterior PDF of $\boldsymbol{\theta}$ conditional on the measured data $\mathcal{D}$ consisting of the IRFs extracted from ambient noise measurements, e.g.,

$$\mathcal{D} = \begin{Bmatrix} S(z_1, t_1) & S(z_1, t_2) & \cdots & S(z_1, t_{N_t}) \\ S(z_2, t_1) & S(z_2, t_2) & \cdots & S(z_2, t_{N_t}) \\ \vdots & \vdots & \ddots & \vdots \\ S(z_{N_o}, t_1) & S(z_{N_o}, t_2) & \cdots & S(z_{N_o}, t_{N_t}) \end{Bmatrix} \tag{6}$$

where N_t is the number of data points for a single observation; $p(\boldsymbol{\theta})$ is the prior PDF of $\boldsymbol{\theta}$; $p(\mathcal{D}|\boldsymbol{\theta})$ is the likelihood function which gives a measure of the agreement between the extract and the predicted IRFs.

3.1.1. Likelihood function

Let us model the prediction error $\boldsymbol{\epsilon}(t) \in \mathbb{R}^{N_o \times 1}$ as the discrepancy between the measured IRFs ($\mathbf{S}(t) \in \mathbb{R}^{N_o \times 1}$) and the predicted IRFs $\left(\hat{\mathbf{S}}(\boldsymbol{\theta}, t) \in \mathbb{R}^{N_o \times 1}\right)$, namely, $\boldsymbol{\epsilon}(t) = \hat{\mathbf{S}}(\boldsymbol{\theta}, t) - \mathbf{S}(t)$, where

$$\begin{aligned} \boldsymbol{\epsilon}(t) &= \left\{ \epsilon(z_1, t), \epsilon(z_2, t), \ldots, \epsilon\left(z_{N_o}, t\right) \right\}^T \\ \mathbf{S}(t) &= \left\{ S(z_1, t), S(z_2, t), \ldots, S\left(z_{N_o}, t\right) \right\}^T \\ \hat{\mathbf{S}}(t) &= \left\{ \hat{S}(\boldsymbol{\theta}, z_1, t), \hat{S}(\boldsymbol{\theta}, z_2, t), \ldots, \hat{S}\left(\boldsymbol{\theta}, z_{N_o}, t\right) \right\}^T \end{aligned} \tag{7}$$

Since the IRFs considered in the model updating are in the time domain, we heuristically assume that $\boldsymbol{\epsilon}$ is modeled as a discrete zero-mean Gaussian process based on the Maximum Entropy Principle (MEP) [52,53]. Under the assumption of equal variances and stochastic independence for the prediction errors of different channels [54], the prediction error follows

$\boldsymbol{\epsilon} \sim \mathcal{N}(\mathbf{0}, \boldsymbol{\Sigma})$ with $\boldsymbol{\Sigma} = \sigma^2\mathbf{I}$. Hence, the likelihood function can be written as

$$p(\mathcal{D}|\boldsymbol{\theta}, \sigma^2) = \left(\frac{1}{2\pi\sigma^2}\right)^{N_o N_t/2} \exp\left(-\frac{1}{2\sigma^2} J(\boldsymbol{\theta})\right) \tag{8}$$

where σ^2 is an additional unknown parameter which denotes the variance of the prediction error; $\mathcal{N}(\cdot, \cdot)$ represents the normal distribution function; $\mathbf{I} \in \mathbb{R}^{N_o \times N_o}$ is an identity matrix; $J(\boldsymbol{\theta})$ is the *goodness-of-fit* function, expressed as

$$J(\boldsymbol{\theta}) = \sum_{j=1}^{N_t} \left\| \hat{\mathbf{S}}(\boldsymbol{\theta}, t_j) - \mathbf{S}(t_j) \right\|_2^2 \tag{9}$$

where $\|\cdot\|_2$ denotes the ℓ_2 (Euclidean) norm.

Noteworthy, recent Bayesian OMA studies have shown that model prediction error in the frequency domain based on the asymptotics of Fourier transform of stochastic processes has a stronger foundation compared to the time domain modeling under MEP assumption [18]. Hence, the likelihood function could be alternatively modeled as complex Wishart distribution in terms of spectral density matrix estimators [18,55] for model updating (e.g, the observed spectral density matrix can be easily obtained from the extracted IRFs in this study). Nevertheless, an inevitable loss in the frequency domain error modeling is that the phase information (e.g., wave propagation) is completely missing. Therefore, to establish a rigorous formulation for Eq. (8) without heuristic assumption, a comprehensive study is needed for the error propagation analysis of the likelihood modeling with IRFs in the time domain, which is beyond the scope of this paper.

3.1.2. Priors

Given an admissible initial stiffness matrix ($\mathbf{K}_0$), the eateries of the unknown model parameters (θ_l) in Eq. (3) have sparsity characteristics (e.g., with zero, positive and/or negative values). To promote the sparsity of the model parameters, we adopt a Laplace prior for each θ_l ($l = 1, 2, \ldots, N_\theta$) [56], given by

$$p(\theta_l|\lambda) = \frac{\lambda}{2}\exp(-\lambda|\theta_l|) \tag{10}$$

where λ is the parameter of the Laplace distribution ($\lambda > 0$) called the regularization parameter. Note that λ becomes another unknown parameter in the Bayesian updating process. Assuming the parameter priors are independent from each other, the prior distribution of $\boldsymbol{\theta}$ can be written as

$$p(\boldsymbol{\theta}|\lambda) = \prod_{l=1}^{N_\theta} p(\theta_l|\lambda) = \left(\frac{\lambda}{2}\right)^{N_\theta} \exp(-\lambda \| \boldsymbol{\theta} \|_1) \tag{11}$$

where $\|\cdot\|_1$ denotes the ℓ_1 (Taxicab) norm. Since σ^2 and λ are always positive, their prior distributions can be modeled by an inverse Gamma and a Gamma distribution, respectively: $p(\sigma^2) \sim \mathcal{G}^{inv}(\alpha, \beta)$ and $p(\lambda) \sim \mathcal{G}(a, b)$, where α, β, a, b are positive constant hyperparameters, defined as [29]

$$p(\sigma^2|\alpha, \beta) = \frac{\beta^\alpha}{\Gamma(\alpha)}\sigma^{-2(\alpha+1)}\exp\left(-\frac{\beta}{\sigma^2}\right) \tag{12}$$

$$p(\lambda|a, b) = \frac{b^a}{\Gamma(a)}\lambda^{a-1}\exp(-b\lambda) \tag{13}$$

where $\mathcal{G}(\cdot, \cdot)$ and $\mathcal{G}^{inv}(\cdot, \cdot)$ denote the Gamma and the inverse Gamma distribution function, respectively, and $\Gamma(\cdot)$ is the Gamma function. In addition, the hyperparameters are fixed to be small so that approximate noninformative priors hold (e.g., in our experiments, we choose $\alpha = a = 1 \times 10^{-3}$ and $\beta = b = 1 \times 10^{-6}$).

3.1.3. Hierarchical bayesian inference

Following the hierarchical Bayesian modeling framework [37,53], we obtain the augmented posterior PDF for unknown parameters $\{\boldsymbol{\theta}, \sigma^2, \lambda\}$ as follows

$$p(\boldsymbol{\theta}, \sigma^2, \lambda|\mathcal{D}) \propto p(\mathcal{D}|\boldsymbol{\theta}, \sigma^2)p(\boldsymbol{\theta}|\lambda)p(\sigma^2|\alpha, \beta)p(\lambda|a, b) \tag{14}$$

The substitution of Eqs. (8), (11)–(13) into Eq. (14) leads to the final form of the posterior PDF:

$$p(\boldsymbol{\theta}, \sigma^2, \lambda|\mathcal{D}) \propto \lambda^{n_2}\left(\frac{1}{\sigma^2}\right)^{n_1} \exp\left\{-\frac{1}{\sigma^2}\left[\frac{J(\boldsymbol{\theta})}{2} + \beta\right] - \lambda(\| \boldsymbol{\theta} \|_1 + b)\right\} \tag{15}$$

where $n_1 = N_o N_t/2 + \alpha + 1$ and $n_2 = N_\theta + a - 1$.

Note that the total number of unknown parameters to be updated is $N_\theta + N_o + 1$. Since Eq. (15) cannot be analytically solved, we herein proposed to use the Gibbs algorithm to sequentially sample the unknown parameters [29] for the

representation of the posterior distributions. The model parameters $\boldsymbol{\theta}$ can be sampled using the Metropolis–Hastings algorithm proposed in Section 3.2, while σ^2 and λ can be sampled from their conditional posterior PDFs analytically derived from Eq. (15), given by

$$\{\sigma^2|\boldsymbol{\theta}, \mathcal{D}, \alpha, \beta\} \sim \mathcal{G}^{inv}\left(\frac{N_o N_t}{2} + \alpha, \frac{J(\boldsymbol{\theta})}{2} + \beta\right) \tag{16}$$

$$\{\lambda|\boldsymbol{\theta}, a, b\} \sim \mathcal{G}\left(N_\theta + a, \| \boldsymbol{\theta} \|_1 + b\right) \tag{17}$$

Following Eqs. (16) and (17), σ^2 and λ can be easily sampled as $\boldsymbol{\theta}$ is given.

3.2. Parameter sampling using Markov chain Monte Carlo simulation

Since the posterior distributions are usually complicated in a normalized form as shown in Eq. (4), it is difficult to directly draw independent samples using classic Monte Carlo (MC) methods. However, the Markov chain MC (e.g., MCMC) makes possible to draw dependent sequences of samples representing the posterior samples. The MCMC simulation is typically regarded as a convenient choice for parameter sampling, which is able to produce a stationary distribution as close to the target distribution as possible.

The Metropolis–Hastings (M–H) algorithm, as an alternative MCMC approach, provides a simple sampling procedure for numerical implementation. The salient feature of this algorithm is to draw samples with an acceptance and rejection rate governed by a probability. Let us assume that random samples are generated from a target distribution $\pi(\boldsymbol{\theta})$. For example, $\pi(\boldsymbol{\theta})$ can be the posterior PDF of the model parameters, e.g., $p(\boldsymbol{\theta}|\sigma^2, \lambda, \mathcal{D})$. Following a rejection sampling procedure, the M–H algorithm generates a sequence of samples $\boldsymbol{\theta}^{(p)}$ from the target distribution. At a generic pth iteration, a candidate solution $\boldsymbol{\theta}^*$ is generated based on the current value $\boldsymbol{\theta}^{(p-1)}$, sampled from a transition proposal $g\left(\boldsymbol{\theta}^*|\boldsymbol{\theta}^{(p-1)}\right)$ [37]. A Bernoulli trial is then performed with a success probability written as

$$\gamma = \min\left\{\frac{\pi(\boldsymbol{\theta}^*)g\left(\boldsymbol{\theta}^{(p-1)}|\boldsymbol{\theta}^*\right)}{\pi\left(\boldsymbol{\theta}^{(p-1)}\right)g\left(\boldsymbol{\theta}^*|\boldsymbol{\theta}^{(p-1)}\right)}, \quad 1\right\} \tag{18}$$

If the trial is successful (e.g., $r_0 \le \gamma$ with r_0 being a uniform random number sampled from [0,1]), $\boldsymbol{\theta}^{(p)}$ is replaced by $\boldsymbol{\theta}^*$; otherwise (e.g., $r_0 > \gamma$), $\boldsymbol{\theta}^{(p)}$ is set to be $\boldsymbol{\theta}^{(p-1)}$. The successful/unsuccessful state is called moving/staying. The rejection sampling process is repeated for a sufficient number of iterations, until the resulting Markov chain becomes stationary. The stationary samples are then used to represent the target (posterior) distribution. The corresponding non-stationary and stationary processes are called the "burn-in" and the "retained" period.

We apply a Cauchy distribution-based transition proposal to generate samples since its PDF has a longer tail which helps alleviate local minima stagnation in sampling [57]. Each candidate can be generated following $\theta_l^* \sim C(\theta^{(p-1)}, \kappa_l)$ with the PDF written as follows

$$g\left(\theta_l^*|\theta_l^{(p-1)}\right) = \frac{1}{\pi\kappa_l}\left[1 + \left(\frac{\theta_l^* - \theta_l^{(p-1)}}{\kappa_l}\right)^2\right]^{-1} \tag{19}$$

where $C(\cdot, \cdot)$ denotes the Cauchy distribution function, κ_l ($l = 1, 2, \ldots, N_\theta$) is the random walk step (tuning parameter) which controls the width of the distribution. Note that, instead of using a fixed value, κ_l can be determined "on the fly" along with the chain generation [58,59]. For example, starting with an initial value of κ_l, we multiply κ_l by 1.01 if a candidate sample is accepted in the "burn-in" period, and divide it by 1.007 when a candidate is rejected [58]. In the "retained" period, we apply a fixed value of κ_l obtained from the end of the "burn-in" period. In this paper, we sample the model parameters $\boldsymbol{\theta}$, the perdition error variance σ^2 and the prior regularization parameter λ sequentially based on the framework of Gibbs sampling [29] together with the M–H algorithm. The proposed MCMC sampler for Bayesian model updating is summarized in Algorithm 1.

Algorithm 1. MCMC sampler using the M–H algorithm and Gibbs sampling for model updating.

input: the prescribed chain length N_{mc}, the burn-in period length N_b, the initial guess for the model parameters $\boldsymbol{\theta}^{(0)}$, the initial random walk step $\kappa_l^{(0)}(l = 1, 2, \ldots, N_\theta)$, the mass information of the structure $\mathbf{M}$, the substructure stiffness matrix $\mathbf{K}_l$, the extract IRFs $\mathbf{S}(t)$ from measurements, and the hyperparameters α, β, a, b.

Output: the chains of samples for parameters $\boldsymbol{\theta}$, σ^2 and λ.

1: Sample the prediction error variance $\left\{\sigma^{2(0)}|\boldsymbol{\theta}^{(0)}, \mathcal{D}, \alpha, \beta\right\} \sim \mathcal{G}^{inv}\left(N_o N_t/2 + \alpha, J\left(\boldsymbol{\theta}^{(0)}\right)/2 + \beta\right)$;

2 Sample the regularization parameter $\left\{\lambda^{(0)}|\boldsymbol{\theta}^{(0)}, a, b\right\} \sim \mathcal{G}\left(N_\theta + a, \left\|\boldsymbol{\theta}^{(0)}\right\|_1 + b\right)$;

3 Initialize the chain index $p \leftarrow 0$;

4 **while** $p < N_{mc}$ **do**

Update the chain index $p \leftarrow p + 1$;
Set $l \leftarrow 1$;
while $l < N_\theta$ **do**
Set $\boldsymbol{\theta}^{(p-1)} \leftarrow \left\{ \theta_1^{(p)}, \ldots, \theta_{l-1}^{(p)}, \theta_l^{(p-1)}, \theta_{l+1}^{(p-1)}, \ldots, \theta_{N_\theta}^{(p-1)} \right\}$;
Sample the candidate solution $\theta_l^* \sim C\left(\theta_l^{(p-1)}, \kappa_l^{(p-1)}\right)$;
Set $\boldsymbol{\theta}^* \leftarrow \left\{ \theta_1^{(p)}, \ldots, \theta_{l-1}^{(p)}, \theta_l^*, \theta_{l+1}^{(p-1)}, \ldots, \theta_{N_\theta}^{(p-1)} \right\}$;
Compute the rejection probability: $\gamma = \exp\left\{ -\frac{1}{2\sigma^{2(p-1)}}\left[J\left(\boldsymbol{\theta}^* - J\left(\boldsymbol{\theta}^{(p-1)}\right)\right] - \lambda^{(p-1)}\left(\|\boldsymbol{\theta}^*\|_1 - \left\|\boldsymbol{\theta}^{(p-1)}\right\|_1 \right) \right\}$
Generate a uniform random number $r_0 \sim U(0, 1)$;
if $r_0 \le \gamma$ **then**
Set $\boldsymbol{\theta}^{(p)} \leftarrow \boldsymbol{\theta}^*$ and $\kappa_l^{(p)} \leftarrow 1.01\kappa_l^{(p-1)}$;
else
Set $\boldsymbol{\theta}^{(p)} \leftarrow \boldsymbol{\theta}^{(p-1)}$ and $\kappa_l^{(p)} \leftarrow \kappa_l^{(p-1)}/1.007$;
end
if $p \ge N_b$ **then**
Set $\kappa_l^{(p)} \leftarrow \kappa_l^{(N_b)}$;
end
Set $l \leftarrow l + 1$;
end
Sample the prediction error variance $\left\{ \sigma^{2(p)} | \boldsymbol{\theta}^{(p)}, \mathcal{D}, \alpha, \beta \right\} \sim \mathcal{G}^{inv}\left(N_o N_t/2 + \alpha, J\left(\boldsymbol{\theta}^{(p)}\right)/2 + \beta \right)$;
Sample the regularization parameter $\left\{ \lambda^{(p)} | \boldsymbol{\theta}^{(p)}, a, b \right\} \sim \mathcal{G}\left(N_\theta + a, \left\|\boldsymbol{\theta}^{(p)}\right\|_1 + b \right)$;
end

4. Experimental example: a 21-storey building at the MIT campus

We test the performance of the proposed algorithm for continuous monitoring and probabilistic model updating of a tall building using field measurements. The instrumented building considered herein is called the Green Building located at the campus of Massachusetts Institute of Technology (MIT) in Cambridge, MA, USA. In this section, we focus on processing the ambient noise measurements and updating a finite element model of this building.

4.1. Description of the Green Building and its instrumentation

The Green Building (see Fig. 2(a)) is an academic building numbered 54 at MIT, which is home to the lab, office, and classroom space of the Department of Earth and Planetary Sciences. The Green Building, currently the tallest building in Cambridge, was designed by I.M. Pei and constructed during the period of 1962–1964. The Green Building is 83.7 m tall (see Fig. 2(b)) with a footprint of 16.5 m by 34 m (see Fig. 2(c)). The short edges of the building are aligned at about 25° north-west [60,61]. The short and long directions of the Green Building are accordingly referred to as North-South (NS) and East-West (EW). As shown in Fig. 2, the ground floor of the Green Building has an open area. The first floor is about 7.1 m above the grade (grade level=6.1 m above sea level) and houses a large lecture hall with mezzanines (the total storey height of about 8.2 m). Mechanical rooms are located on the top two floors (e.g., 19th and 20th floors). Heavy meteorological and radio equipments are asymmetrically mounted on the roof (see Fig. 2(a)), e.g., a radome is mounted on the south-west corner [60]. Three elevator shafts are located on the eastern side of the building (see Fig. 2(c)) and two stairwells are placed symmetrically at the NE and NW corners of the building. The building is constructed of cast-in-place reinforced concrete. The eastern and western façades are composed of 0.25 m thick shear walls running the height of the building. The thickness of floor slabs is typically 0.1016 m. The Green Building has a basement with an elevation of 3.8 m below the grade.

As illustrated in Fig. 3, the Green Building is instrumented by the United States Geological Survey (USGS) with 36 uniaxial EpiSensor ES-US force balance accelerometers designed by Kinemetrics Inc., CA, USA, for structural monitoring. The sensor sampling rate is 200 Hz on a 24 bit digitizer with a recording range of ± 4 g. The data recorder is the Granite model as shown in Fig. 3. The accelerometers are connected by cables to a central data recording station and synchronized using the global positioning system (GPS) with a discrepancy of less than 1 μs. The system is connected by internet and set to trigger if acceleration magnitudes over 0.001 g (about 0.01 m/s^2) are detected. Acceleration data can also be collected through on-demand recordings and real-time monitoring [60]. The sensor array was designed for monitoring the NS and EW translational vibration, the torsion, and the base rocking motion. The sensor locations and orientations are shown in Fig. 3. Note that the accelerometers are installed below the floor slabs.

Fig. 4 illustrates the sensor locations at a typical floor. For each floor, the storey accelerations (u_o for EW direction, v_o for

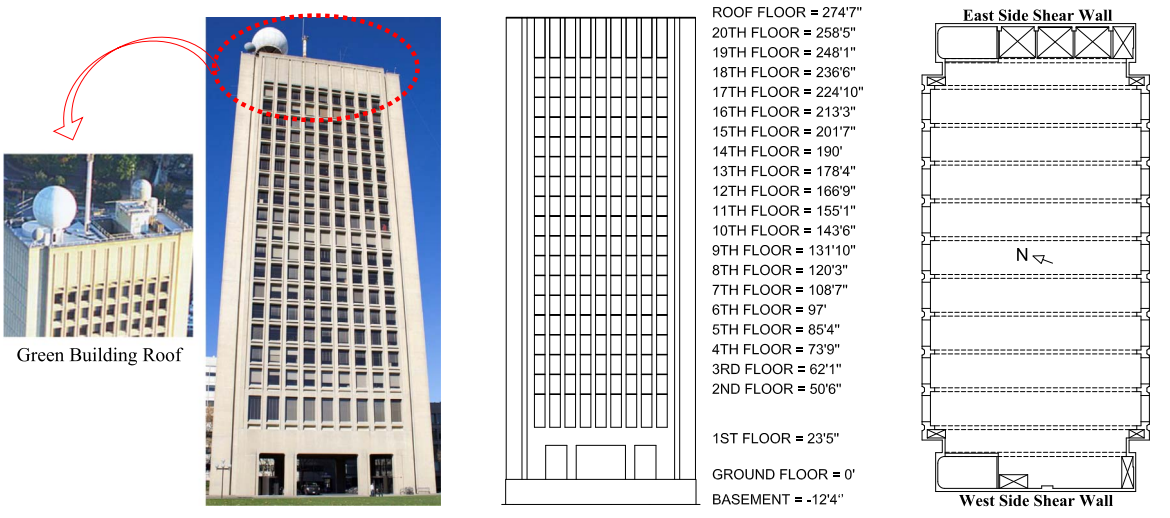

(a) Green Building (b) South façade elevation view (c) A typical floor plan

Fig. 2. Green Building at the MIT campus. Note that the east and west sides are concrete shear walls. (a) Green Building (b)South façade elevation view (c) A typical floor plan.

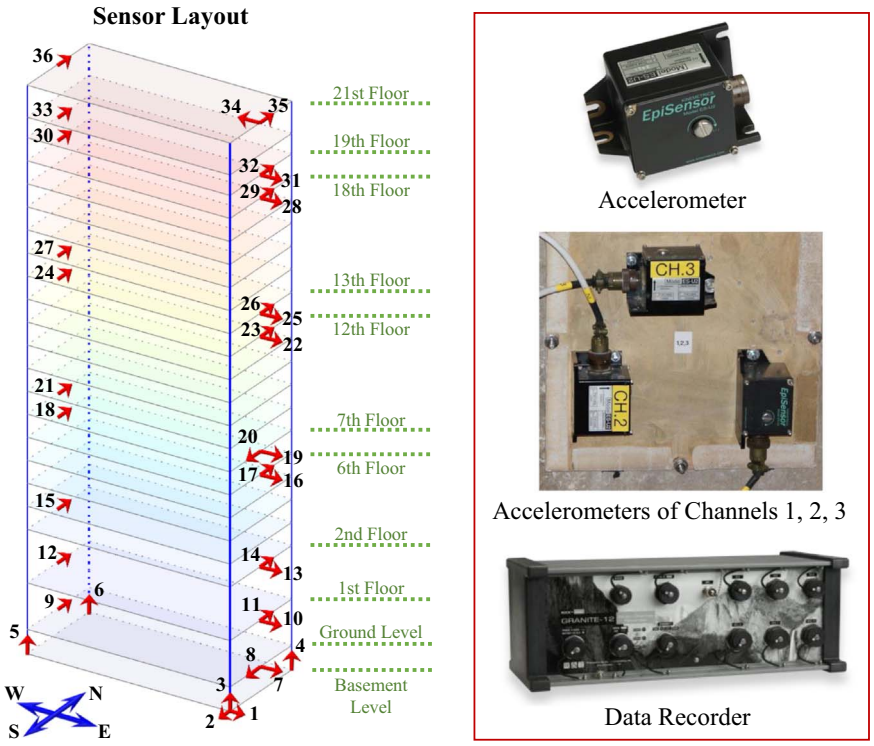

Fig. 3. Instrumentation of the Green Building. The accelerometers are installed below the floor slabs. (For interpretation of the references to color in this figure legend, the reader is referred to the web version of this article.)

NS direction and θ_o for torsional direction as shown in Fig. 4) can be computed using the following equations

$$u_1 = u_o - \theta_o y_1$$
$$v_1 = v_o + \theta_o x_1$$
$$v_2 = v_o + \theta_o x_2 \quad (20)$$

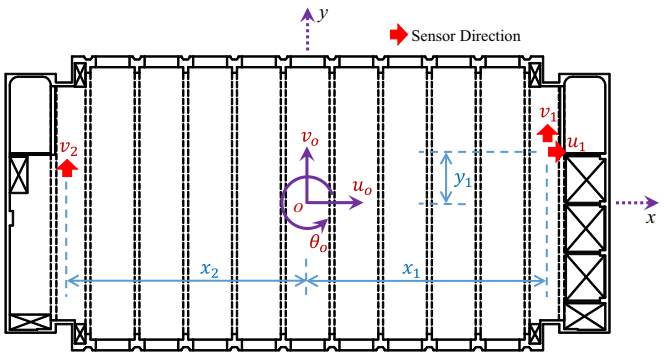

Fig. 4. Sensor locations at a typical floor. Here, u_1, v_1 and v_2 denote the measured accelerations, while u_o, v_o and θ_o denote the derived accelerations at the reference pint $O = (0, 0)$. (For interpretation of the references to color in this figure legend, the reader is referred to the web version of this article.)

Table 1
Sensor coordinates with respect to selected reference point O.

Floor level	x_1 (m)	x_2 (m)	y_1 (m)	Floor level	x_1 (m)	x_2 (m)	y_1 (m)
Ground	14.08	−13.98	5.99	12 FL	13.93	−15.11	2.29
1 FL	16.50	−16.50	3.49	13 FL	16.50	−15.11	3.19
2 FL	16.50	−16.50	3.49	18 FL	13.93	−15.21	2.32
6 FL	13.93	−15.21	2.29	19 FL	13.93	−15.17	2.32
7 FL	13.93	−15.21	2.29	21 FL	16.75	−16.75	3.32

where u_1 is the measured acceleration along the EW direction, v_1 and v_2 are the measured accelerations along the NS direction close to the eastern and western shear walls respectively, x_1, x_2 and y_1 are the sensor coordinates in the x-O-y coordinate system with $O = (0, 0)$ shown in Fig. 4. Table 1 shows the sensor coordinates with respect to selected reference point O of the Green Building.

4.2. Deconvolution analysis of the ambient noise measurements

The monitoring system of the Green Building operated continuously and collected acceleration data for 15 days (e.g., between 12 and 27 May 2015) under ambient noise conditions. Hence, we have 15 days of continuous ambient noise records at each sensor. We herein only consider the NS horizontal measurements to validate the proposed approach. The measurements of the EW and the torsional directions can be analyzed similarly. To wit, we take the storey accelerations v_o calculated from Eq. (20) for analysis.

4.2.1. Observed records and data pre-processing

Fig. 5 illustrates the root mean square (RMS) amplitude computed over a 30 s moving window of the raw data along the NS direction for 15 days. It can be seen that the RMS amplitudes change over time (e.g., higher RMS amplitudes are observed on May 12th, 13th, 20th, 22nd, etc.). The temporal variations of the RMS amplitudes might be induced by human activities, elevators, computers, lab equipments inside the building, air conditioners, environmental effects such as wind, and other sources. Fig. 6 shows the power spectrum density (PSD) functions for a typical set of one hour ambient measurement along

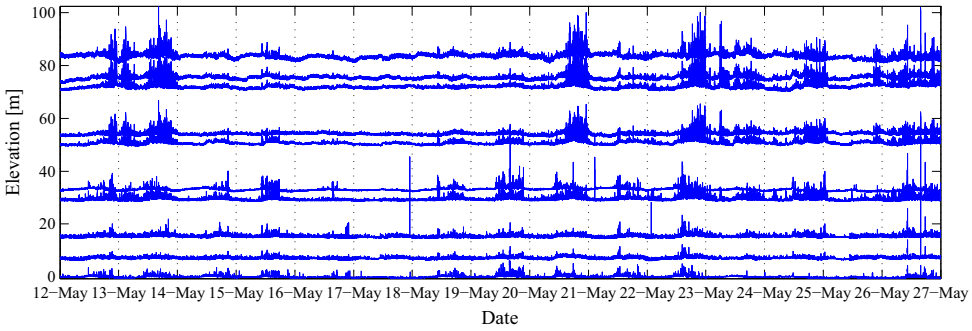

Fig. 5. Root mean square (RMS) amplitude plot of the 15-day continuous ambient noise measurements of the Green Building along the NS direction. Note that the RMS time series are calculated based on 30-s moving windows of the raw records.

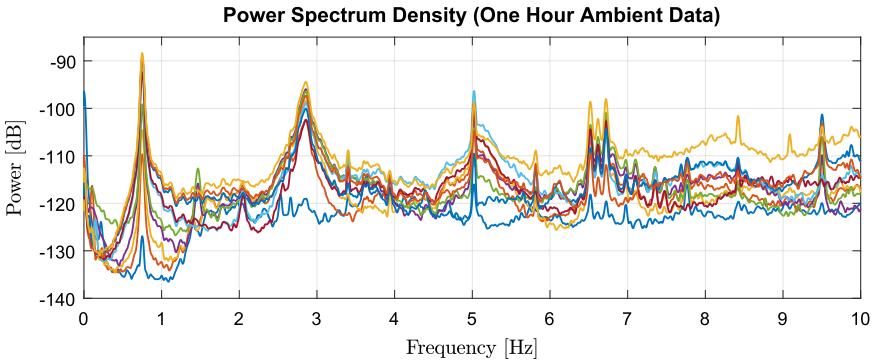

Fig. 6. Power spectrum density (PSD) functions for a typical set of one hour ambient measurement along the NS direction. Note that the curves in different colors represent different floor levels. To compute the PSD, the time domain signals are divided into 10.24 s windows with 25% overlap and averaging is applied to the PSD windows. (For interpretation of the references to color in this figure legend, the reader is referred to the web version of this article.)

the NS direction.

After down-sampling the data to 100 Hz, we divide the 15-d records into 20 min windows (overlapping 50%) to obtain reliable IRFs and de-trend the data in each window. Since we focus on ambient vibrations of the building, signals with large amplitudes are excluded from the continuous records in the process of deconvolution analysis [23]. For instance, some sensors placed under stairs and close to the elevator shafts of the Green Building record large amplitude local vibrations due to human interference and/or mechanical equipments functioning. To obtain much more reasonable ambient noise measurements for IRFs extraction, we apply a data-weighting technique to clip large amplitude data based on the threshold value which is identical to 1.5 times the standard deviation of the window records for each station [23,62]. Records with amplitude larger than the threshold value are replaced by the threshold value.

4.2.2. Extraction of IRFs

We apply Eq. (1) to extract the IRFs for each 20-min window and "stack" (average) them over the 15-d period. Each window is deconvolved with respect to the ground floor. The averaged IRFs represent the shear waveforms subjected to a unit impulse ground motion. When the stack of the IRFs become stable, adding more time would not significantly change the features of the waveforms [26]. We employ a low-pass filter with a cutoff frequency of 8 Hz to the averaged IRFs and obtain the travel waves as shown in Fig. 7. It can be seen that the waves clearly prorogate upward and downward in both positive and negative times which correspond to causal and acausal waves, respectively, excited by multiple sources inside and outside the building [23]. Mathematically, the waveforms of IRFs shown in Fig. 7 can be explained as follows: given an impulse excitation at the source location (ground level) of the building at $t=0$, the responses (e.g., IRFs) at upper floors are obtained. As illustrated by the arrows in Fig. 7, the pulse travels up in the building, is totally reflected at the roof, then travels down where it is reflected on the ground, and goes up again.

From the IRFs, we can measure several characteristics of the building, such as the wave velocity, the resonant frequencies and the attenuation parameters like damping ratios. By measuring the travel time of the pulse inside the building, we can assess its traveling speed. For example, the travel time of the wave from the ground to the roof is about $t_v = 0.23$ s within a distance of $H = 83.7$ m. Therefore, the wave speed is estimated to be $V = 364$ m/s (e.g., H/t_v). The uncertainty of the wave speed estimation can be also quantified using least squares fitting through estimating the travel times at different floors [23,26]. By tracking the change of the shear wave velocity, we can detect possible damage and disturbance of the building as well as interpret the environmental effect on structural monitoring [63].

In addition, the resonant frequencies can be well obtained through peak picking of the power spectrum of the IRFs. For example, the first two resonant frequencies of the Green Building are $f_1 = 0.745$ Hz and $f_2 = 2.843$ Hz which match the results reported in [61]. We also estimate damping ratios corresponding to the first two resonant frequencies. Fig. 8 shows the Frequency response functions (FRFs) of the extracted IRFs and the least squares linear curve fitting for the envelopes of the filtered IRFs for the first two modes. The average half-power bandwidth around a certain dominant frequency is firstly computed and the "-3 dB" frequencies are obtained for bandpass filtering (see Fig. 8(a)). The filtered IRFs are then used for damping determination. It can be seen from Fig. 8(b) and (c) as well as the cov_μ values that the curve fitting for the first mode is better than that for the second mode. The damping ratios for the first two modes can be calculated using Eq. (2), v.i.z., $\xi_1 = 2.66\%$ and $\xi_2 = 2.82\%$. The frequencies and damping ratios for the first two modes are then used to model the damping matrix in the model updating process as illustrated in Section 4.3. In addition, mode shapes of the first two modes can be obtained through peaking the values of the filtered storey IRFs at $t = 0$ as given in Fig. 9.

It is noteworthy that the great advantage of using ambient noise measurements for the deconvolution interferometry analysis is that ambient vibrations can be recorded continuously, everywhere and at any time so that we do not need to rely on controlled (artificial) or natural (earthquakes) sources. They, thus, allow non-invasive and non-destructive testing and monitoring of structures such as buildings.

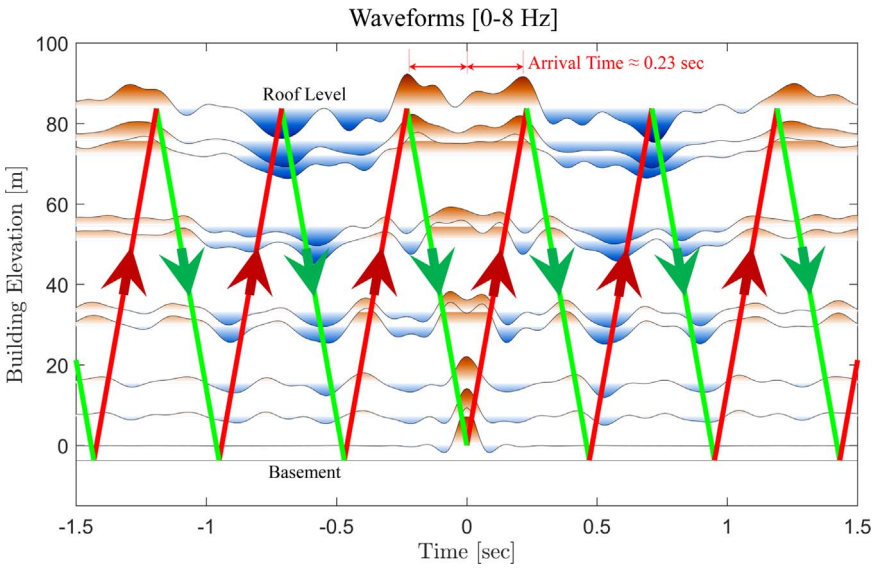

Fig. 7. Filtered IRFs (impulse response functions) for the frequency range of 0–8 Hz calculated from 15-day ambient noise measurements along the NS direction. The red and green arrows represent waves traveling upward (positive slope) and downward (negative slope), respectively. The wave travel time is about 0.23 s at the roof level and the corresponding shear wave velocity is about 364 m/s. (For interpretation of the references to color in this figure legend, the reader is referred to the web version of this article.)

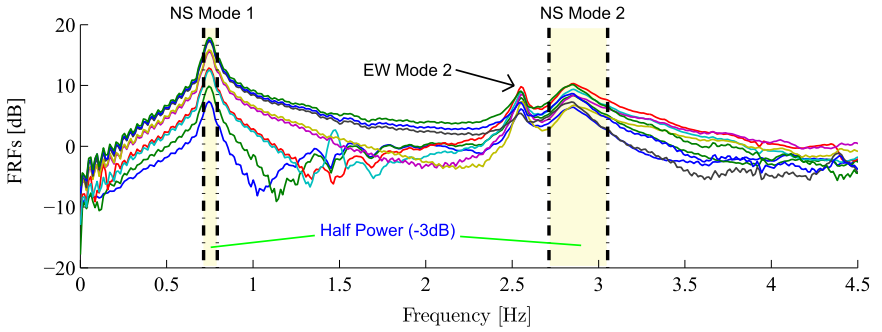

(a) Frequency response functions (FRFs) and the half-power bandwidths for the first two modes

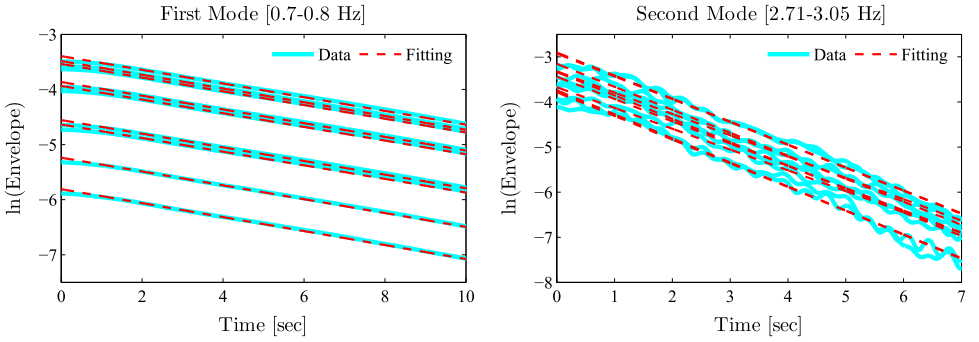

(b) $|\bar{\mu}| = 0.1246$ and $\mathrm{cov}_{\mu} = 0.82\%$ (c) $|\bar{\mu}| = 0.5039$ and $\mathrm{cov}_{\mu} = 4.75\%$

Fig. 8. Curve fitting for the envelopes of the filtered IRFs for the first two modes. The shaded area denotes the half-power bandwidth for a dominant frequency. Note that the FRF curves in (a) and the curves from the bottom to the top in (b) and (c) represent different floor levels, $\bar{\mu}$ denotes the mean slope of the fitted lines and cov_{μ} denotes the corresponding coefficient of variance. (a) Frequency response functions (FRFs) and the half-power bandwidths for the first two modes (b) $|\bar{\mu}|=0.1246$ and $\mathrm{cov}_{\mu}=0.82\%$ (c) $|\bar{\mu}|=0.5039$ and $\mathrm{cov}_{\mu}=4.75\%$. (For interpretation of the references to color in this figure legend, the reader is referred to the web version of this article.)

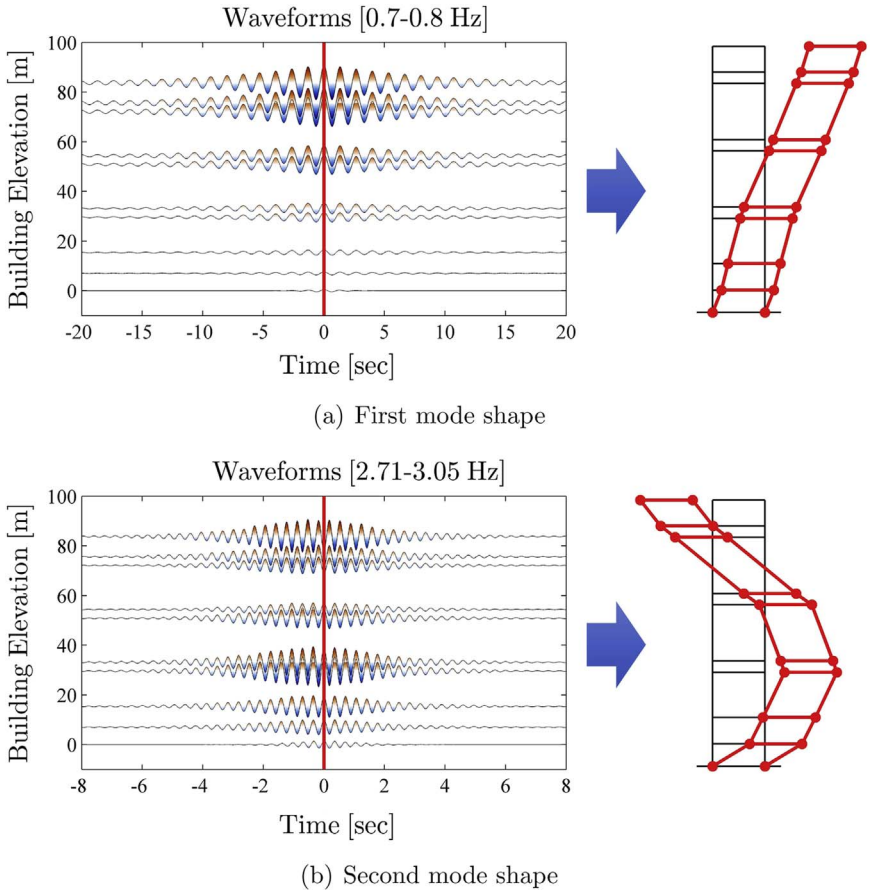

Fig. 9. Extracted mode shapes of the Green Building through filtering the IRFs. The mode shape values are obtained through peaking the filtered IRFs values at zero time ($t=0$). Note that the IRFs are filtered around the corresponding dominant frequencies. (a) First mode shape (b) Second mode shape. (For interpretation of the references to color in this figure legend, the reader is referred to the web version of this article.)

4.3. Model updating of the Green Building

We update the finite element model of the Green Building using Bayesian framework based on the extracted IRFs discussed in Section 4.2.2. The purpose of updating the building model against field measurements is to initiate a baseline model for structural response prediction subjected to potential extreme events and for damage detection/quantification in future operations. Note that the predicted IRFs at different floors (e.g., $\hat{S}(\boldsymbol{\theta}, z_i, t)$, $i = 1, 2, \ldots, 9$) can be simulated by solving the dynamic equations of the model with the input setting to be the impulse ground motion (e.g., $S(z_0, t)$). The long enough ambient noise measurements (e.g., 15 days in this study) promise to provide a great resolution for structural parameters to be updated. In regard to temporal (continuous) monitoring of a building, the IRFs can be extracted every 15 days and the model is updated accordingly (e.g. for possible damage quantification).

4.3.1. Finite element modeling of the Green Building

An initial finite element model of the Green Building is established using ETABS (Computers and Structures, Inc., CA, USA) based on its architectural and structural drawings as partially shown in Fig. 2. Stone concrete with a compressive strength of 27.6 MPa and density of 2400 kg/m^3 is used to construct the columns and exterior walls, while lightweight concrete with a compressive strength of 25.9 MPa and density of 2000 kg/m^3 is used for slabs, beams and stairs. Interior partitions such as interior walls are also included in the finite element model, whose density is set to be 900 kg/m^3 and stiffness is set to be 1% of that of the stone concrete. Therefore, the interior partitions primarily contribute to the mass. Fig. 10 shows the full scale finite element model of the Green Building with a list of several typical floor plans. We model the Green Building with a fixed base on the ground while excluding the basement of the building. This assumption simplifies the modeling but ignores the soil-structure interaction effect on the building motion. However, for low-amplitude vibrations such as ambient vibrations, such an effect can be ignorable [2].

We assume that the floor diaphragms are rigid in plane and masses can be lumped at the center of mass each floor. Then the lumped mass matrix ($\mathbf{M}$) and the initial translational stiffness matrix ($\mathbf{K}_0$) can be extracted from the full scale finite element model for the NS direction. $\mathbf{K}_0$ is obtained following the standard procedure below: 1) for the lth storey of the

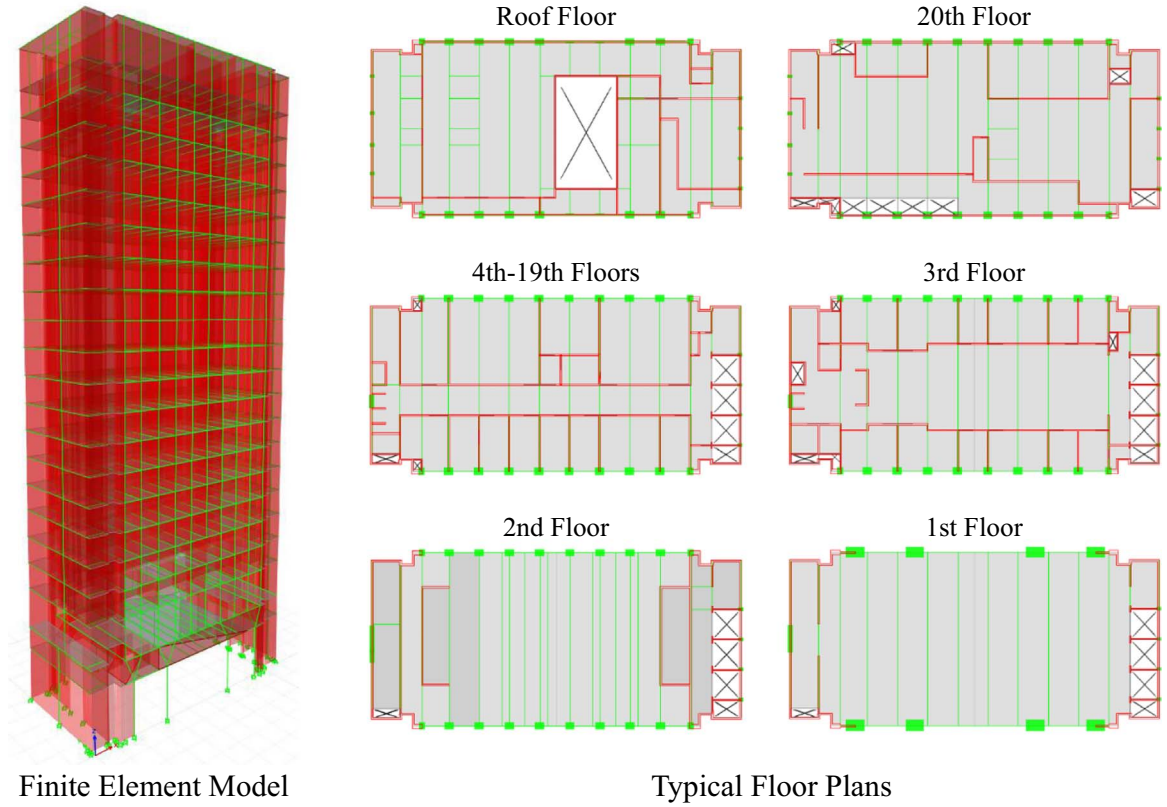

Fig. 10. Green Building full scale finite element model. (For interpretation of the references to color in this figure legend, the reader is referred to the web version of this article.)

building model ($l = 1, 2, \ldots, 21$), apply a unit load at the center of floor mass, run the finite element analysis, and record the jth storey displacement (note that $j \le l$); 2) construct an upper triangular matrix using the storey displacement recorded in the previous step with l and j representing the column and the row of the matrix, respectively; 3) convert the upper triangular matrix to a full matrix (called the flexibility matrix denoted with $\mathbf{D}$) based on matrix symmetry; 4) compute the inverse of $\mathbf{D}$ and set it to be the initial stiffness matrix, e.g., $\mathbf{K}_0 = \mathbf{D}^{-1}$. The lumped storey masses of the Green Building extracted from the finite element model are given as follows: $m_1 = 965$, $m_2 = 851$, $m_3 = 464$, $m_4 = 478$, $m_5 \sim m_{18} = 487$, $m_{19} = 461$, $m_{20} = 511$ and $m_{21} = 443$ ton.

The first two dominant frequencies of the initial model are 0.825 (10.74%) and 3.297 (15.96%) Hz, where the percentage values in the parentheses represent the discrepancies between the analytical frequencies and those of the measured data. The discrepancy illustrates that the analytical model cannot accurately represent the actual building due to idealized model assumptions and inaccurate structural information. Therefore, we carry out updating of the Green Building model to achieve an analytical model which yields responses as close as possible to the actual measurements. We apply a shear type model to describe the substructure (e.g., $\mathbf{K}_l (l = 1, 2, \ldots, 21)$ in Eq. (3)) of the Green Building for the NS direction and have totally 21 stiffness parameters to update, e.g., $\boldsymbol{\theta} = \{k_1, k_2, \ldots, k_{21}\}^T$. To predict the IRFs using the finite element model, the formulation of damping matrix is required. However, in real application it is not necessary to determine the damping matrix for modal analysis and damping ratios can be directly identified from data. We herein apply a Rayleigh damping to model the attenuation mechanism of the Green Building, namely, $\mathbf{C} = \alpha_r \mathbf{M} + \beta_r \mathbf{K}$, where α_r and β_r are two damping coefficients which can be determined by the modal damping ratios and the natural frequencies of two selected vibrational modes. Herein α_r and β_r can be approximately predetermined before model updating using the two estimated damping ratios ($\xi_1 = 2.66\%$ and $\xi_2 = 2.82\%$) and frequencies ($f_1 = 0.745$ Hz and $f_2 = 2.843$ Hz) in Section 4.2.2, namely, $\alpha_r = 0.200$ and $\beta_r = 2.543 \times 10^{-3}$. Though the Rayleigh damping involves modeling error in real applications, it has been frequently used in time domain structural response prediction [64,65].

4.3.2. Model updating results

We apply the proposed Bayesian model updating approach (see Algorithm 1) to quantify the uncertainty of the 21 stiffness parameters. The IRFs in the positive time filtered by a band-pass filter (0.1–15 Hz) are used in the model updating process. The essential parameters for the MCMC sampler used for the simulation are given as follows: $N_{mc} = 2 \times 10^5$, $N_b = 6 \times 10^4$, $\kappa_l^{(0)} = 0.005$, $\alpha = a = 1 \times 10^{-3}$ and $\beta = b = 1 \times 10^{-6}$. The lower and upper bounds for the stiffness parameters

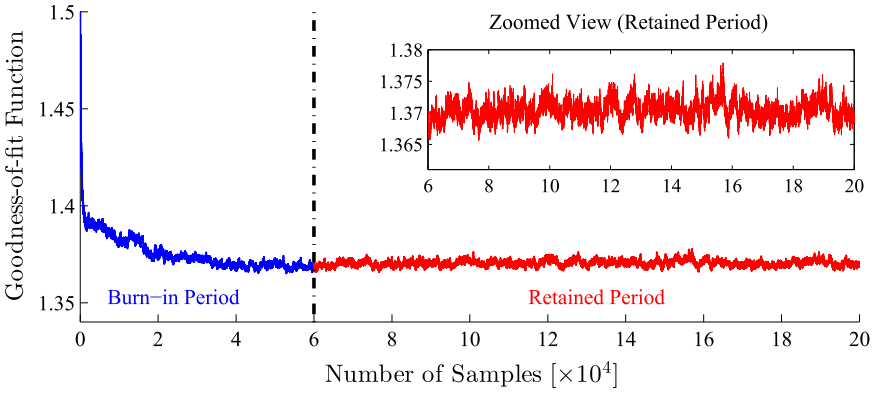

Fig. 11. MCMC convergence of the *goodness-of-fit function*. (For interpretation of the references to color in this figure legend, the reader is referred to the web version of this article.)

are -5×10^9 and 1×10^{10} N/m, respectively. The numerical analyses are programmed in MATLAB® (The MathWorks, Inc., MA, USA) on a standard Intel (R) Core (TM) i7-4930 K 3.40 GHz PC with 32 G RAM.

Fig. 11 shows the convergence of the goodness-of-fit function as presented in Eq. (9). It is seen that the algorithm converges after about 4×10^4 iterations. After "burn-in", the goodness-of-fit function becomes stationary as illustrated in the zoomed view of the "retained" period in Fig. 11. Similar convergence can be observed in the parameter samples, for example, Fig. 12 gives the Markov chains of several stiffness parameters sampled by the proposed MCMC model updating algorithm. In general, stationary samples can be observed in the "retained" period as shown in Fig. 12. The "burn-in" period of 3×10^4 iterations are sufficient and the "retained" samples can be used for the representation of the posterior distributions of the stiffness parameters. Fig. 13 depicts the pairwise plots of posterior samples for some typical stiffness parameters. It can be seen that some of the stiffness parameters approximately follow the normal distribution (e.g., the regions of the k_2-k_3, k_5-k_6, k_9-k_{10} and k_{13}-k_{14} pairwise samples are similar to ellipses).

Fig. 14 shows the quantified posterior PDFs of the 21 stiffness parameters for the Green Building model. It is noted that the posterior PDFs, represented by histograms, are obtained based on the statistics of the samples in the "retained" period. We also fit the posterior histograms using the generalized extreme value (GEV) distribution. It is seen from Fig. 14 that the fitted GEV curves can represent the posterior parameter distributions quite well, e.g., the GEV curves match the histograms quite well. The maximum *a posteriori* (MAP) estimate of the stiffness parameters (e.g., $\hat{k}_l$, where $l = 1, 2, \ldots, 21$) as well as the 90% confidence intervals are also summarized in Fig. 14. The MAP estimates of the first two dominant frequencies are 0.730 (2.0%) and 2.836 (0.2%) Hz, where the percentage values in the parentheses mean the relative errors between the updated analytical frequencies and the measured frequencies, showing a satisfactory model updating performance of the proposed algorithm. Noteworthy, the quantified PDFs for the stiffness parameters can be used as the baseline distributions for possible damage (e.g., post-earthquake damage) and disturbance detection of the building in the future.

In addition, Fig. 15 illustrates the identified PDFs of the prediction error variance σ^2 and the regularization parameter λ. It

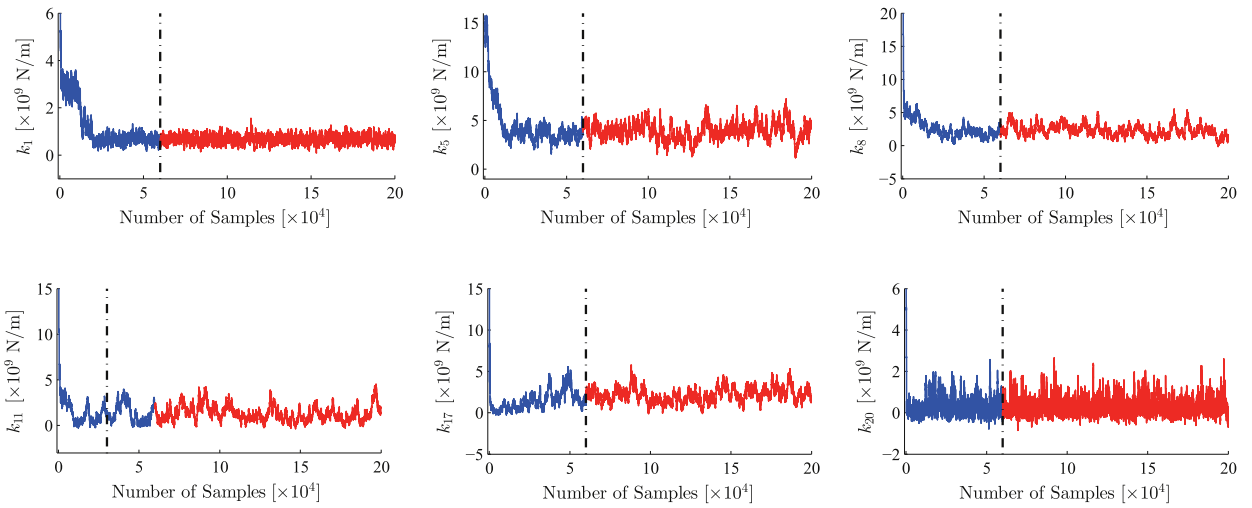

Fig. 12. Markov chains of several stiffness parameters sampled by the MCMC model updating algorithm. (For interpretation of the references to color in this figure legend, the reader is referred to the web version of this article.)

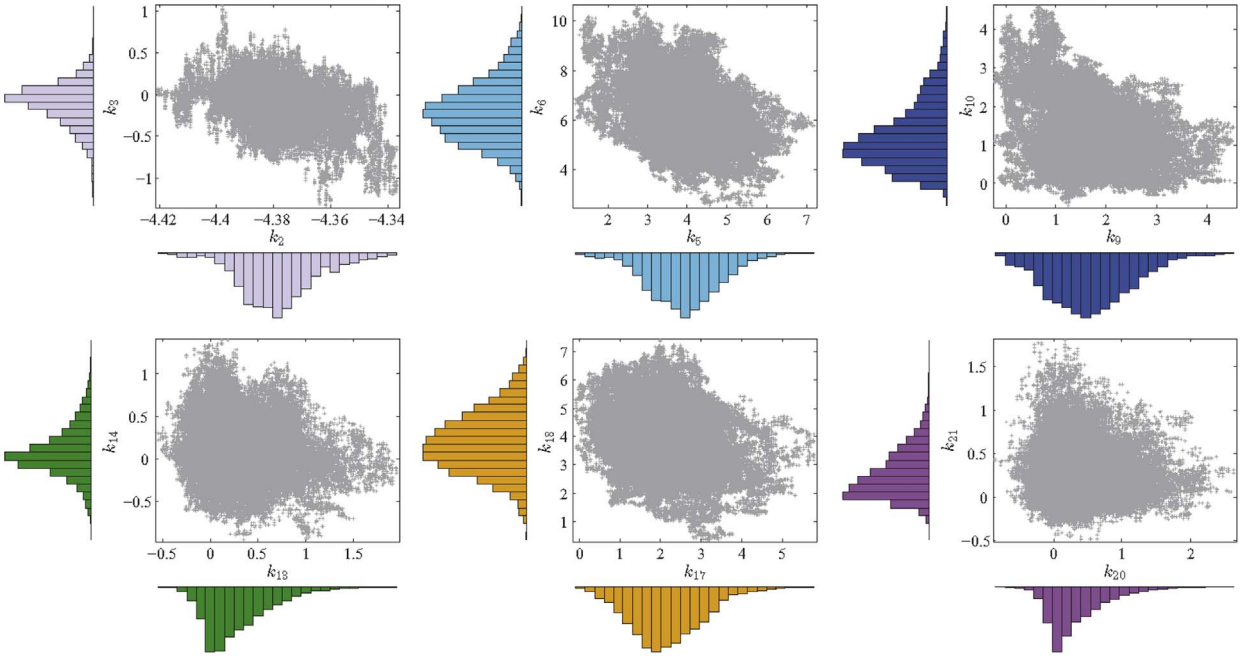

Fig. 13. Pairwise plots of posterior samples ("retained" period samples of the MCMC) for some stiffness parameters. Note that the unit for the stiffness parameters in this figure is 1×10^9 N/m. (For interpretation of the references to color in this figure legend, the reader is referred to the web version of this article.)

is seen that the PDFs have small deviations. Since both σ^2 and λ are positive, the log-normal distribution is used to fit their posterior histograms. It can be observed from Fig. 15 that the fitted log-normal curves perfectly agree with the posterior histograms. The MAP estimate of those two parameters are $\hat{\sigma}^2 = 1.521 \times 10^{-4}$ and $\hat{\lambda} = 64.3$. Fig. 16 shows the reconstructed IRFs in the positive time of the Green Building in comparison with the IRFs extracted from 15 day continuous measurements through deconvolution. The reconstructed IRFs are calculated from simulation using the initial model and the updated model with the MAP estimate of the stiffness parameters, respectively. It can be seen from Fig. 16 that the reconstructed IRFs obtained by the initial model have large discrepancies compared with the measured IRFs. After model updating, the reconstructed IRFs can agree with the measured IRFs quite well. Fig. 17 shows the reconstructed FRF of a typical floor compared with the measured FRF. In general, the reconstructed spectrum of the updated model matches the measured one well excluding the region around 5 Hz. Nevertheless, the frequency of about 5 Hz can be obviously seen as the second torsional mode of the Green Building through analyzing the torsional measurements. Since we only consider model updating of the NS translational direction of the Green Building in this example, it appears reasonable that reconstructed spectrum does not fit the torsional mode. Overall, the proposed algorithm performs quite well for probabilistic updating of the model stiffness parameters.

5. Conclusions

We present a novel computational approach for continuous monitoring of buildings using seismic interferometry and ambient noise measurements. A 21-storey concrete building, called the Green Building, located at the MIT campus is studied to validate the proposed approach. We retrieve the travel waves inside the building through deconvolving the storey records with respect to the ground measurement (virtual source). Unlike the deconvolution of earthquake records, the ambient measurements are divided into overlapping windows and deconcolved window-by-window. Temporal averaging over a long enough duration is applied to the IRFs (impulse response functions) for each window so as to obtain the representative IRFs of the building. Note that the IRF represents the representative building response to an input delta function at the ground floor. Since numerous inside and outside sources simultaneously excite the building, the IRFs are presented in both positive and negative times, corresponding to causal and acausal waves, respectively. From the extracted IRFs, we can measure the building characteristics, such as the wave velocity, resonant frequencies, mode shapes and damping ratios. In addition, since the interferometric analyses of ambient data for different channels are independent from each other, distributed computing can be applied to obtain the IRFs. Though it is nice to show the wave propagation inside a building based on the IRFs, this method requires a sufficiently long data set to remove the source effect using temporal averaging, which places a limitation of applying this approach to short period ambient measurements.

To connect the IRFs to the building mechanical characteristics, we characterize and update a finite element model of the

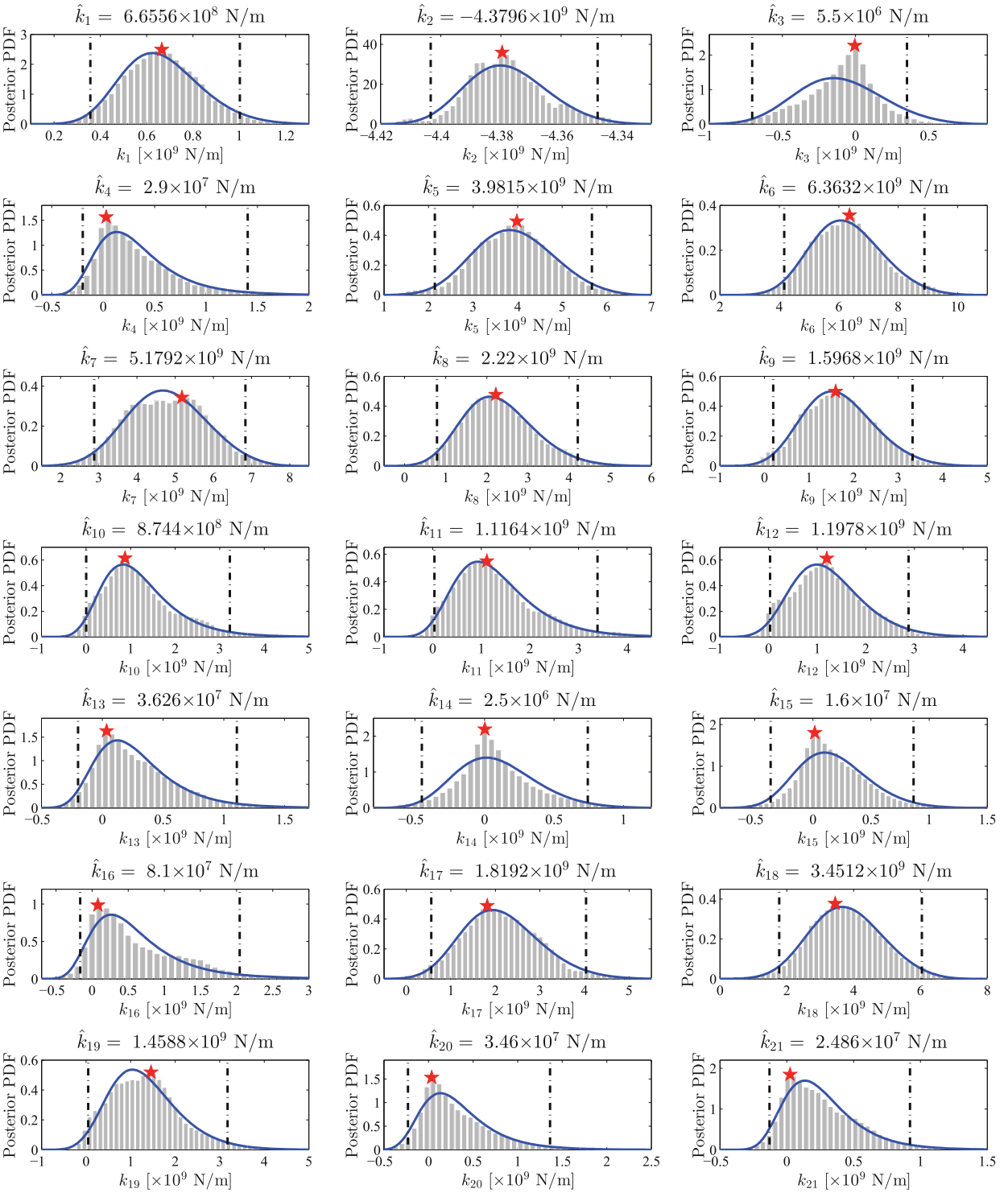

Fig. 14. Identified stiffness parameter PDFs of the Green Building model using 15 day continuous measurements. Note that the histograms denote the PDFs obtained from MCMC sampling and the solid blue lines denote the PDFs through curve fitting using the generalized extreme value (GEV) distribution. The red star denotes the maximum *a posteriori* estimate $\hat{k}_l$, where $l = 1, 2, \ldots, 21$. The dash-dot lines represent the 90% confidence interval. (For interpretation of the references to color in this figure legend, the reader is referred to the web version of this article.)

Green Building against the extracted building responses using the Bayesian model updating approach. We parameterize the model by 21 stiffness parameters and quantify the parameter uncertainties using a Markov chain Monte Carlo sampling technique with adaptive random-walk steps. The priors of the stiffness parameters are modeled by the Laplace distribution

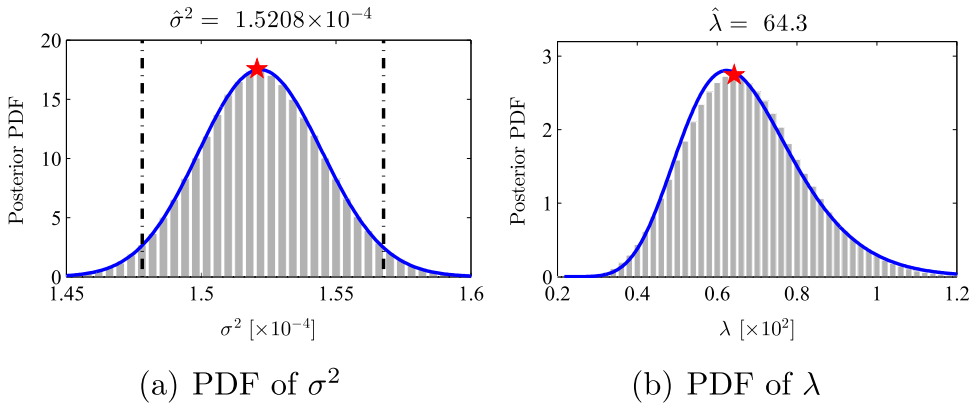

Fig. 15. Identified PDFs of the prediction error variance σ^2 and the regularization parameter λ. Note that the histograms denote the PDFs obtained from MCMC sampling and the solid blue lines denote the PDFs through curve fitting using the log-normal distribution. The red star denotes the maximum a posteriori estimate $\hat{\sigma}^2$ and $\hat{\lambda}$. (a) PDF of σ^2 (b)PDF of λ. (For interpretation of the references to color in this figure legend, the reader is referred to the web version of this article.)

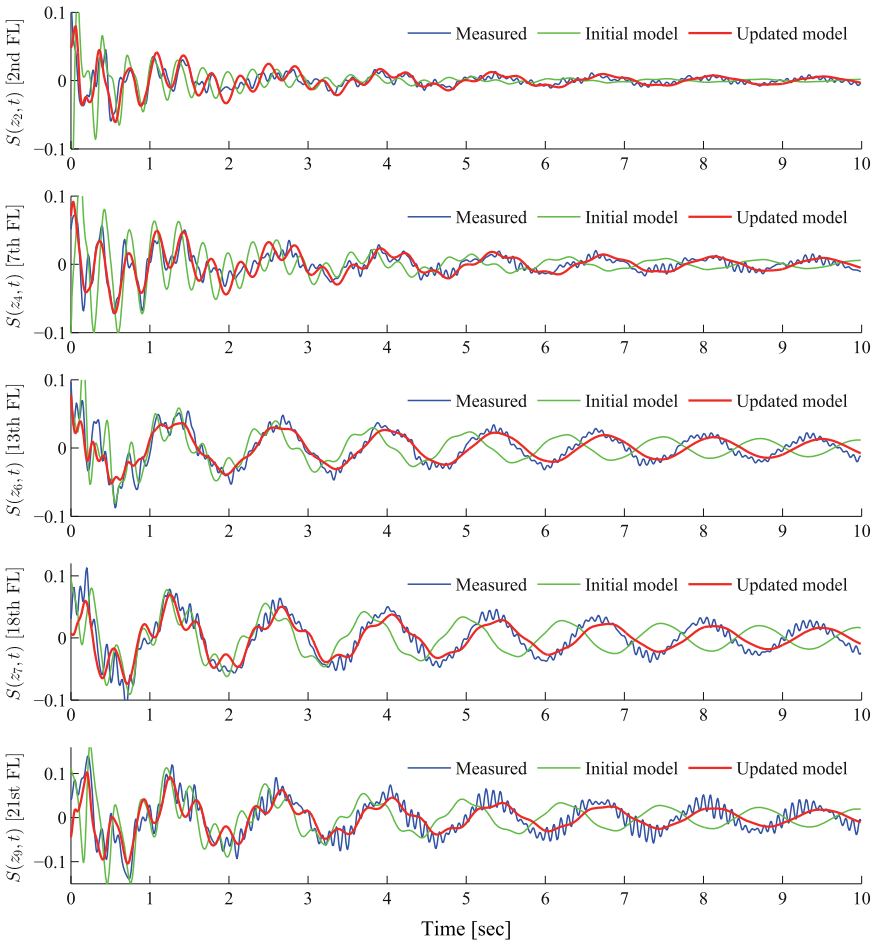

Fig. 16. Example of reconstructed IRFs (impulse response functions) of the Green Building in comparison with the IRFs extracted from 15 day continuous measurements by deconvolution. Note that the reconstructed IRFs are obtained from simulation using the initial model and the updated model with the maximum *a posteriori* parameter estimate. (For interpretation of the references to color in this figure legend, the reader is referred to the web version of this article.)

which brings the Bayesian inference with ℓ_1 sparse regularization. The updated model with quantified parameter uncertainties can be used as a baseline for future damage (e.g., post-earthquake damage) or disturbance detection. In general, the results show the effectiveness of the proposed approach for response extraction and probabilistic model updating of

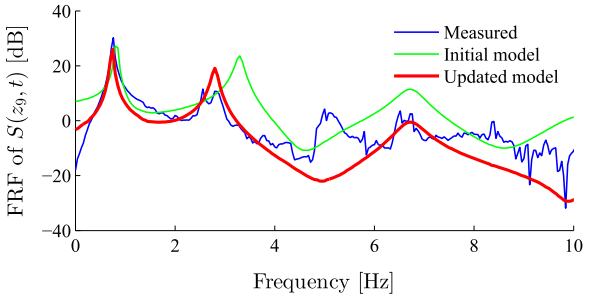

Fig. 17. A typical reconstructed frequency response function (FRF) compared with the FRF extracted from 15 day continuous measurements. Note that the reconstructed FRF is computed based on the initial model and the updated model with the maximum *a posteriori* parameter estimate. Note that the frequency component of about 5 Hz in the measured FRF is a torsional resonant frequency of the Green Building. (For interpretation of the references to color in this figure legend, the reader is referred to the web version of this article.)

buildings. The Bayesian updating process is able to link the interferometric analysis results to the model properties of a building, providing a possible way to quantify the building performance and health condition. In addition, the methodology described here allows for continuous temporal health monitoring and post-earthquake damage detection of buildings.

Acknowledgments

The authors would like to acknowledge the support by the Royal Dutch Shell through the MIT Energy Initiative. We also acknowledge the partial support by the Kuwait-MIT Signature Project through the Kuwait Foundation for the Advancement of Sciences and the Kuwait-MIT Center for Natural Resources and the Environment. The Green Building was instrumented by the support of the United States Geological Survey. The authors would also like to acknowledge the anonymous reviewers for their constructive comments which helped in improving the quality of the paper.

References

[1] M.D. Kohler, P.M. Davis, E. Şafak, Earthquake and ambient vibration monitoring of the steel-frame UCLA factor building, Earthq. Spectra 21 (3) (2005) 715–736.
[2] D. Skolnik, Y. Lei, E. Yu, J.W. Wallace, Identification, model updating, and response prediction of an instrumented 15-story steel-frame building, Earthq. Spectra 22 (3) (2006) 781–802.
[3] M.I. Todorovska, M.D. Trifunac, Impulse response analysis of the van nuys 7-storey hotel during 11 earthquakes and earthquake damage detection, Struct. Control Health Monit. 15 (1) (2008) 90–116.
[4] A.L. Hong, R. Betti, C.-C. Lin, Identification of dynamic models of a building structure using multiple earthquake records, Struct. Control Health Monit. 16 (2) (2009) 178–199.
[5] R. Omrani, R.E. Hudson, E. Taciroglu, Story-by-story estimation of the stiffness parameters of laterally-torsionally coupled buildings using forced or ambient vibration data: II. application to experimental data, Earthq. Eng. Struct. Dyn. 41 (12) (2012) 1635–1649.
[6] Y.-C. Liu, C.-H. Loh, Y.-Q. Ni, Stochastic subspace identification for output-only modal analysis application to super high-rise tower under abnormal loading condition, Earthq. Eng. Struct. Dyn. 42 (4) (2013) 477–498.
[7] M.P. Limongelli, Seismic health monitoring of an instrumented multistory building using the interpolation method, Earthq. Eng. Struct. Dyn. 43 (11) (2014) 1581–1602.
[8] D.M. Siringoringo, Y. Fujino, Long-term seismic monitoring of base-isolated building with emphasis on serviceability assessment, Earthq. Eng. Struct. Dyn. 44 (4) (2015) 637–655.
[9] D. Bindi, B. Petrovic, S. Karapetrou, M. Manakou, T. Boxberger, D. Raptakis, K. Pitilakis, S. Parolai, Seismic response of an 8-story RC-building from ambient vibration analysis, Bull. Earthq. Eng. 13 (7) (2015) 2095–2120.
[10] Y. Kaya, S. Kocakaplan, E. Şafak, System identification and model calibration of multi-story buildings through estimation of vibration time histories at non-instrumented floors, Bull. Earthq. Eng. 13 (11) (2015) 3301–3323.
[11] B. Peeters, G.D. Roeck, Reference-based stochastic subspace identification for output-only modal analysis, Mech. Syst. Signal Process. 13 (6) (1999) 855–878.
[12] R. Brincker, L. Zhang, P. Andersen, Modal identification of output-only systems using frequency domain decomposition, Smart Mater. Struct. 10 (3) (2001) 441–445.
[13] W. Zhou, D. Chelidze, Blind source separation based vibration mode identification, Mech. Syst. Signal Process. 21 (8) (2007) 3072–3087.
[14] K.-V. Yuen, J.L. Beck, L.S. Katafygiotis, Probabilistic approach for modal identification using non-stationary noisy response measurements only, Earthq. Eng. Struct. Dyn. 31 (4) (2002) 1007–1023.
[15] S.-K. Au, Fast Bayesian ambient modal identification in the frequency domain, part I posterior most probable value, Mech. Syst. Signal Process. 26 (2012) 60–75.
[16] S.-K. Au, Fast Bayesian ambient modal identification in the frequency domain, part II posterior uncertainty, Mech. Syst. Signal Process. 26 (2012) 76–90.
[17] S.-K. Au, F.-L. Zhang, Y.-C. Ni, Bayesian operational modal analysis theory, computation, practice, Comput. Struct. 126 (2013) 3–14.
[18] S.-K. Au, Insights on the Bayesian spectral density method for operational modal analysis, Mech. Syst. Signal Process. 66–67 (2016) 1–12.
[19] W.-J. Yan, L.S. Katafygiotis, A two-stage fast Bayesian spectral density approach for ambient modal analysis. part I posterior most probable value and uncertainty, Mech. Syst. Signal Process. 54–55 (2015) 139–155.
[20] W.-J. Yan, L.S. Katafygiotis, A two-stage fast Bayesian spectral density approach for ambient modal analysis. part II mode shape assembly and case studies, Mech. Syst. Signal Process. 54–55 (2015) 156–171.
[21] R. Snieder, E. Şafak, Extracting the building response using seismic interferometry theory and application to the Millikan library in Pasadena,

California, Bull. Seismol. Soc. Am. 96 (2) (2006) 586–598.
[22] M.D. Kohler, T.H. Heaton, S.C. Bradford, Propagating waves in the steel, moment-frame factor building recorded during earthquakes, Bull. Seismol. Soc. Am. 97 (4) (2007) 1334–1345.
[23] N. Nakata, R. Snieder, Monitoring a building using deconvolution interferometry. II ambient-vibration analysis, Bull. Seismol. Soc. Am. 104 (1) (2014) 204–213.
[24] M. Ebrahimian, M. Rahmani, M.I. Todorovska, Nonparametric estimation of wave dispersion in high-rise buildings by seismic interferometry, Earthq. Eng. Struct. Dyn. 43 (15) (2014) 2361–2375.
[25] M. Rahmani, M.I. Todorovska, 1d system identification of a 54-story steel frame building by seismic interferometry, Earthq. Eng. Struct. Dyn. 43 (4) (2014) 627–640.
[26] G.A. Prieto, J.F. Lawrence, A.I. Chung, M.D. Kohler, Impulse response of civil structures from ambient noise analysis, Bull. Seismol. Soc. Am. 100 (5A) (2010) 2322–2328.
[27] M. Friswell, J.E. Mottershead, Finite Element Model Updating in Structural Dynamics, Kluwer Academic Publishers, Norwell, USA, 1995.
[28] Y. Lu, Z. Tu, Dynamic model updating using a combined genetic-eigensensitivity algorithm and application in seismic response prediction, Earthq. Eng. Struct. Dyn. 34 (9) (2005) 1149–1170.
[29] J. Ching, M. Muto, J.L. Beck, Structural model updating and health monitoring with incomplete modal data using gibbs sampler, Comput. – Aided Civ. Infrastruct. Eng. 21 (4) (2006) 242–257.
[30] K.-V. Yuen, J.L. Beck, L.S. Katafygiotis, Efficient model updating and health monitoring methodology using incomplete modal data without mode matching, Struct. Control Health Monit. 13 (1) (2006) 91–107.
[31] P.G. Bakir, E. Reynders, G.D. Roeck, Sensitivity-based finite element model updating using constrained optimization with a trust region algorithm, J. Sound Vib. 305 (1–2) (2007) 211–225.
[32] C. Soize, E. Capiez-Lernout, J.-F. Durand, C. Fernandez, L. Gagliardini, Probabilistic model identification of uncertainties in computational models for dynamical systems and experimental validation, Comput. Methods Appl. Mech. Eng. 198 (1) (2008) 150–163.
[33] K. Christodoulou, E. Ntotsios, C. Papadimitriou, P. Panetsos, Structural model updating and prediction variability using pareto optimal models, Comput. Methods Appl. Mech. Eng. 198 (1) (2008) 138–149.
[34] K.-V. Yuen, Updating large models for mechanical systems using incomplete modal measurement, Mech. Syst. Signal Process. 28 (0) (2012) 297–308.
[35] I. Behmanesh, B. Moaveni, G. Lombaert, C. Papadimitriou, Hierarchical Bayesian model updating for structural identification, Mech. Syst. Signal Process. 64–65 (2015) 360–376.
[36] H.-F. Lam, J. Yang, S.-K. Au, Bayesian model updating of a coupled-slab system using field test data utilizing an enhanced markov chain monte carlo simulation algorithm, Eng. Struct. 102 (2015) 144–155.
[37] H. Sun, O. Büyüköztürk, Probabilistic updating of building models using incomplete modal data, Mech. Syst. Signal Process. 75 (0) (2016) 27–40.
[38] C. Mares, J. Mottershead, M. Friswell, Stochastic model updating part 1 – theory and simulated example, Mech. Syst. Signal Process. 20 (7) (2006) 1674–1695.
[39] H. Ahmadian, J. Mottershead, M. Friswell, Regularisation methods for finite element model updating, Mech. Syst. Signal Process. 12 (1) (1998) 47–64.
[40] J.E. Mottershead, M. Link, M.I. Friswell, The sensitivity method in finite element model updating: a tutorial, Mech. Syst. Signal Process. 25 (7) (2011) 2275–2296.
[41] J.D. Sipple, M. Sanayei, Finite element model updating using frequency response functions and numerical sensitivities, Struct. Control Health Monit. 21 (5) (2014) 784–802.
[42] H. Sun, R. Betti, A hybrid optimization algorithm with Bayesian inference for probabilistic model updating, Comput. – Aided Civ. Infrastruct. Eng. 30 (8) (2015) 602–619.
[43] B. Goller, H. Pradlwarter, G. Schuller, Robust model updating with insufficient data, Comput. Methods Appl. Mech. Eng. 198 (37–40) (2009) 3096–3104.
[44] W. Becker, J. Oakley, C. Surace, P. Gili, J. Rowson, K. Worden, Bayesian sensitivity analysis of a nonlinear finite element model, Mech. Syst. Signal Process. 32 (2012) 18–31. (uncertainties in Structural Dynamics).
[45] C. Papadimitriou, D.-C. Papadioti, Component mode synthesis techniques for finite element model updating, Comput. Struct. 126 (2013) 15–28.
[46] H. Jensen, E. Millas, D. Kusanovic, C. Papadimitriou, Model-reduction techniques for Bayesian finite element model updating using dynamic response data, Comput. Methods Appl. Mech. Eng. 279 (2014) 301–324.
[47] K.-V. Yuen, S.-C. Kuok, Online updating and uncertainty quantification using nonstationary output-only measurement, Mech. Syst. Signal Process. 66–67 (2016) 62–77.
[48] S.-K. Au, F.-L. Zhang, Fundamental two-stage formulation for Bayesian system identification,part I general theory, Mech. Syst. Signal Process. 66–67 (2016) 31–42.
[49] F.-L. Zhang, S.-K. Au, Fundamental two-stage formulation for Bayesian system identification, part II application to ambient vibration data, Mech. Syst. Signal Process. 6667 (2016) 43–61.
[50] N. Nakata, R. Snieder, S. Kuroda, S. Ito, T. Aizawa, T. Kunimi, Monitoring a building using deconvolution interferometry. I earthquake-data analysis, Bull. Seismol. Soc. Am. 103 (3) (2013) 1662–1678.
[51] G.D. Bensen, M.H. Ritzwoller, M.P. Barmin, A.L. Levshin, F. Lin, M.P. Moschetti, N.M. Shapiro, Y. Yang, Processing seismic ambient noise data to obtain reliable broad-band surface wave dispersion measurements, Geophys. J. Int. 169 (3) (2007) 1239–1260.
[52] J.L. Beck, L.S. Katafygiotis, Updating models and their uncertainties. i: bayesian statistical framework, J. Eng. Mech. 124 (4) (1998) 455–461.
[53] K.-V. Yuen, Bayesian Methods for Structural Dynamics and Civil Engineering, John Wiley & Sons (Asia) Pte Ltd, Singapore, 2010.
[54] J.L. Beck, K.-V. Yuen, Model selection using response measurements bayesian probabilistic approach, J. Eng. Mech. 130 (2) (2004) 192–203.
[55] K.-V. Yuen, S. Kuok, Bayesian methods for updating dynamic models, Appl. Mech. Rev. 64 (1) (2011) 010802.
[56] N. Dobigeon, A. Hero, J.-Y. Tourneret, Hierarchical Bayesian sparse image reconstruction with application to MRFM, IEEE Trans. Image Process. 18 (9) (2009) 2059–2070.
[57] P. Green, Bayesian system identification of a nonlinear dynamical system using a novel variant of simulated annealing, Mech. Syst. Signal Process. 52–53 (2015) 133–146.
[58] W. Link, R. Barker, Bayesian Inference: with ecological applications, Academic Press, San Diego, CA, 2010.
[59] J. Nichols, W. Link, K. Murphy, C. Olson, A Bayesian approach to identifying structural nonlinearity using free-decay response application to damage detection in composites, J. Sound Vib. 329 (15) (2010) 2995–3007.
[60] P. Trocha, Characterization of structural properties and dynamic behavior using distributed accelerometer networks and numerical modeling, Master thesis, Massachusetts Institute of Technology, Cambridge, 2013.
[61] M. Çelebi, N. Toksöz, O. Büyüköztürk, Rocking behavior of an instrumented unique building on the MIT campus identified from ambient shaking data, Earthq. Spectra 30 (2) (2014) 705–720.
[62] U. Wegler, C. Sens-Schönfelder, Fault zone monitoring with passive image interferometry, Geophys. J. Int. 168 (3) (2007) 1029–1033.
[63] A. Mordret, H. Sun, G.A. Prieto, N. Toksöz, O. Büyüköztürk, Continuous monitoring of high-rise buildings using seismic interferometry, Bulletin of the Seismological Society of America (in submission).
[64] P. Jehel, P. Léger, A. Ibrahimbegovic, Initial versus tangent stiffness-based Rayleigh damping in inelastic time history seismic analyses, Earthq. Eng. Struct. Dyn. 43 (3) (2014) 467–484.
[65] K. Kaynardağ, S. Soyoz, Effect of identification on seismic performance assessment of a tall building, Bulletin of Earthquake Engineering (in press). http://dx.doi.org/10.1007/s10518-015-9836-9.